

X-ray, Optical, and Near-infrared Monitoring of the New X-ray Transient MAXI J1820+070 in the Low/hard State

MEGUMI SHIDATSU,¹ SATOSHI NAKAHIRA,² SATOSHI YAMADA,³ TAIKI KAWAMURO,⁴ YOSHIHIRO UEDA,³ HITOSHI NEGORO,⁵
KATSUHIRO L. MURATA,⁶ RYOSUKE ITOH,⁶ YUTARO TACHIBANA,⁶ RYO ADACHI,⁶ YOICHI YATSU,⁶ NOBUYUKI KAWAI,⁶
HIDEKAZU HANAYAMA,⁷ TAKASHI HORIUCHI,⁷ HIROSHI AKITAYA,⁸ TOMOKI SAITO,⁹ MASAKI TAKAYAMA,⁹
TOMOHIITO OHSHIMA,⁹ NORIYUKI KATOH,⁹ JUN TAKAHASHI,⁹ TAKAHIRO NAGAYAMA,¹⁰ MASAYUKI YAMANAKA,¹¹
MIHO KAWABATA,¹² TATSUYA NAKAOKA,¹² SEIKO TAKAGI,¹³ TOMOKI MOROKUMA,¹⁴ KUMIKO MORIHANA,¹⁵
HIROYUKI MAEHARA,¹⁶ AND KAZUHIRO SEKIGUCHI¹⁷

¹Department of Physics, Ehime University, 2-5, Bunkyocho, Matsuyama, Ehime 790-8577, Japan

²High Energy Astrophysics Laboratory, RIKEN, 2-1, Hirosawa, Wako, Saitama 351-0198, Japan

³Department of Astronomy, Kyoto University, Kitashirakawa-Oiwake-cho, Sakyo-ku, Kyoto, Kyoto 606-8502, Japan

⁴National Astronomical Observatory of Japan, Osawa, Mitaka, Tokyo 181-8588, Japan

⁵Department of Physics, Nihon University, 1-8-14 Kanda-Surugadai, Chiyoda-ku, Tokyo 101-8308, Japan

⁶Department of Physics, Tokyo Institute of Technology, 2-12-1 Ookayama, Meguro-ku, Tokyo 152-8551, Japan

⁷Ishigakijima Astronomical Observatory, National Astronomical Observatory of Japan, National Institutes of Natural Sciences, 1024-1 Arakawa, Ishigaki, Okinawa, 907-0024, Japan

⁸Graduate School of Science and Engineering, Saitama University, Simo-okubo 135, Sakura-ku, Saitama 338-8570, Japan

⁹Nishi-Harima Astronomical Observatory, Center for Astronomy, University of Hyogo, 407-2, Nishigaichi, Sayo, Hyogo, 679-5313, Japan

¹⁰Graduate School of Science and Engineering, Kagoshima University, 1-21-35 Korimoto, Kagoshima 890-0065, Japan

¹¹Hiroshima Astrophysical Science Center, Hiroshima University, Higashi-Hiroshima, Hiroshima 739-8526, Japan

¹²Department of Physical Science, Hiroshima University, Kagamiyama 1-3-1, Higashi-Hiroshima 739-8526, Japan

¹³Department of CosmoSciences, Hokkaido University, Kita 10 Nishi 8, Kita-ku, Sapporo, Hokkaido 060-0810, Japan

¹⁴Institute of Astronomy, Graduate School of Science, The University of Tokyo, 2-21-1, Osawa, Mitaka, Tokyo 181-0015, Japan

¹⁵Graduate School of Science, Nagoya University, Furo-cho, Chikusa-ku, Nagoya 464-8602, Japan

¹⁶Okayama Observatory, Graduate School of Science, Kyoto University, 3037-5 Honjo, Kamogata, Asakuchi, Okayama, 719-0232, Japan

¹⁷National Astronomical Observatory of Japan, National Institutes of Natural Sciences, 2-21-1, Osawa, Mitaka, Tokyo 181-8588, Japan

(Accepted October 17, 2018)

ABSTRACT

We report X-ray, optical, and near-infrared monitoring of the new X-ray transient MAXI J1820+070 discovered with MAXI on 2018 March 11. Its X-ray intensity reached ~ 2 Crab in 2–20 keV at the end of March, and then gradually decreased until the middle of June. In this period, the X-ray spectrum was described by Comptonization of the disk emission, with a photon index of ~ 1.5 and an electron temperature of ~ 50 keV, which is consistent with a black hole X-ray binary in the low/hard state. The electron temperature and the photon index were slightly decreased and increased with increasing flux, respectively. The source showed significant X-ray flux variation on timescales of seconds. This short-term variation was found to be associated with changes in the spectral shape, and the photon index became slightly harder at higher fluxes. This suggests that the variation was produced by a change in the properties of the hot electron cloud responsible for the strong Comptonization. Modeling a multi-wavelength SED around the X-ray flux peak at the end of March, covering the near-infrared to X-ray bands, we found that the optical and near-infrared fluxes were likely contributed substantially by the jet emission. Before this outburst, the source was never detected in the X-ray band with MAXI (with a 3σ upper limit of ~ 0.2 mCrab in 4–10 keV, obtained from the 7-year data in 2009–2016), whereas weak optical and infrared activity was found at their flux levels ~ 3 orders of magnitude lower than the peak fluxes in the outburst.

Keywords: X-rays: individual (MAXI J1820+070) — X-rays: binaries — accretion, accretion disks — black hole physics

1. INTRODUCTION

Transient Galactic black hole binaries (BHBs) provides opportunities to study the evolution of black hole accretion flows over a wide range of mass accretion rates (e.g., McClintock & Remillard 2006; Done et al. 2007, for reviews). They are usually too faint to detect in the X-ray band, but suddenly increase their X-ray luminosity by orders of magnitude on timescales of days to weeks. At low luminosities, they stay in the so-called low/hard state and show a power-law shaped hard spectrum, often with an exponential cutoff at ~ 100 keV. This spectral profile is often interpreted as thermal Comptonization of the soft X-ray photons from the truncated standard disk, in a hot electron cloud developed somewhere around the disk. However, the geometry of the Comptonized region is not yet clear. Moreover, energetic electrons and the synchrotron emission produced in jets may contribute to the Comptonized component, but to what extent they do is still in debate. Multi-wavelength observations are important to tackle these questions, because the main part of the jet synchrotron emission is normally located in the radio to optical band.

MAXI J1820+070 was discovered with the MAXI (Matsuoka et al. 2009)/Gas Slit Camera (GSC; Mihara et al. 2011). The MAXI Nova Search System (Negoro et al. 2016) first triggered the source at 2018 March 11 UT 12:50 (Kawamuro et al. 2018a). Soon after the discovery, the source was associated with the optical variable source, ASSASN-2018ey (Denisenko 2018). The position of the X-ray source was precisely determined in follow-up observations with Swift, as $(\alpha^{2000}, \delta^{2000}) = (18^{\text{h}}20^{\text{m}}21^{\text{s}}.88, +07^{\circ}11'08.''3)$, which was consistent with the position of ASSASN-2018ey.

The relatively small interstellar absorption/extinction, with a hydrogen column density of $\sim 10^{21} \text{ cm}^{-2}$, and the high flux, exceeding 1 Crab in 2–20 keV at the peak, have motivated extensive multi-wavelength follow-up observations of MAXI J1820+070 during the outburst (Kennea et al. 2018; Kennea & Siegel 2018; Kennea 2018; Baglio et al. 2018; Bright et al. 2018; Littlefield 2018; Uttley et al. 2018; Bahramian et al. 2018; Garnavich & Littlefield 2018; Sako et al. 2018; Del Santo & Segreto 2018; Paice et al. 2018; Gandhi et al. 2018a; Trushkin et al. 2018; Tetarenko et al. 2018; Berdyugin et al. 2018; Casella et al. 2018; Mandal et al. 2018a,b; Bozzo et al. 2018; Floers et al. 2018; Munoz-Darias et al. 2018; Mereminskiy et al. 2018; Kuulkers et al. 2018; Russell et al. 2018). Until the middle of June, the

source always showed a power-law shaped X-ray spectrum with a photon index of ~ 1.5 , consistent with BHB spectra in the low/hard state. The source was found to show strong optical and X-ray short-term variability on time scales of less than 1 s (Gandhi et al. 2018a; Sako et al. 2018), and in both X-ray and optical bands, low-frequency quasi periodic oscillations (QPOs) were detected at 10–50 mHz (Gandhi et al. 2018a; Mereminskiy et al. 2018; Yu et al. 2018). Radio counterpart was also detected (Bright et al. 2018; Trushkin et al. 2018; Tetarenko et al. 2018), suggesting the presence of jets. After the X-ray flux decay until the middle of June, the source started to increase its X-ray flux again. Then, it showed an X-ray spectral softening in July, at the flux comparable to the first peak (Homan et al. 2018).

In this article, we investigate the nature of MAXI J1820+070, mainly focusing on the period before the X-ray re-brightening, using X-ray data obtained from monitoring observations with MAXI, Swift, and optical and near-infrared (IR) data from ground-based telescopes participating in the collaboration of Optical and Infrared Synergetic Telescopes for Education and Research (OISTER) in Japan. Throughout this work, we utilized HEASoft version 6.23 for the X-ray data reduction, and XSPEC version 12.10.0 with the solar abundance table given by Wilms et al. (2000) for the spectral analysis. Errors represent the 90% confidence ranges for one parameter, unless otherwise stated.

2. X-RAY DATA

2.1. Observations and data reduction

2.1.1. MAXI data

We reduced the MAXI/GSC event data with the processed version 1.3.6.6, through the MAXI analysis tools implemented in “MAXI/GSC on-demand web interface”¹ (Nakahira et al. 2013). The source events were extracted from a circular region with a radius of $2^{\circ}.0$, centered at the target position. Background events were collected from the source-free region within $3^{\circ}.0$ from the source position, determined by excluding the source region and $2^{\circ}.0$ from nearby bright sources.

Figure 1 shows the MAXI/GSC light curves of MAXI J1820+070 in 2–6 keV and 6–20 keV and their hardness ratios (HRs), together with the Swift/BAT light curve in

¹ <http://maxi.riken.jp/mxondem>

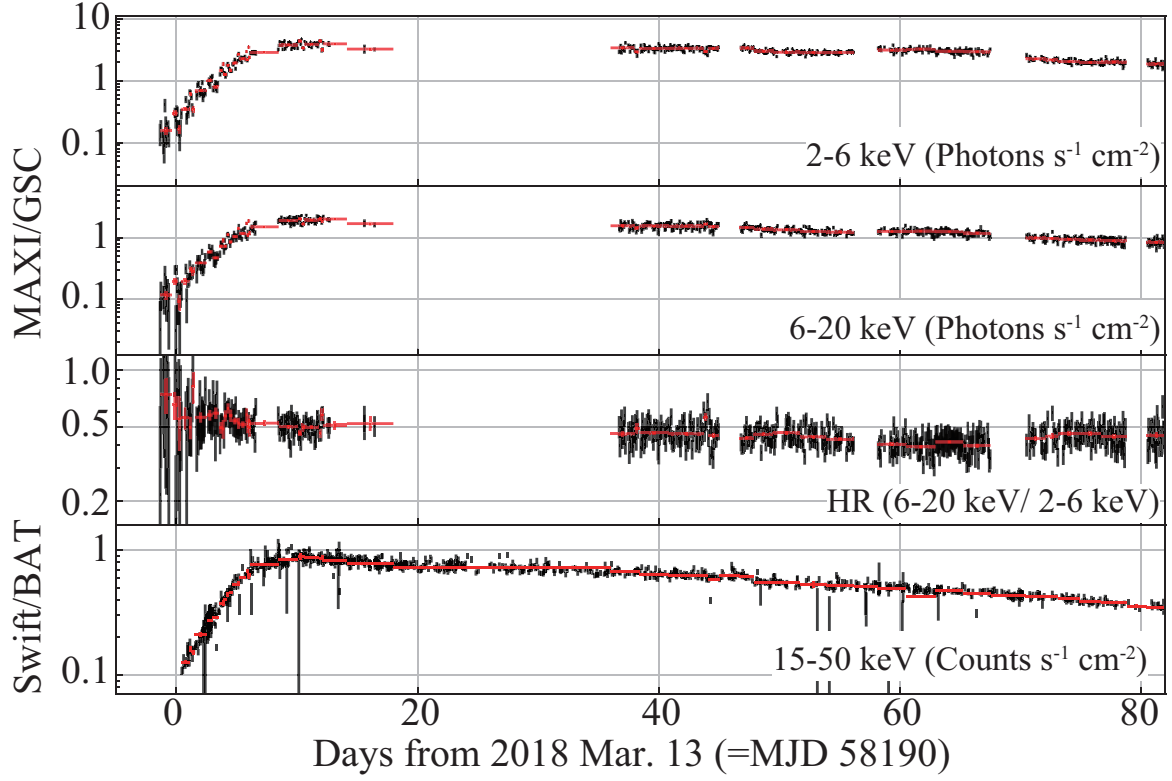


Figure 1. *MAXI/GSC* light curves of MAXI J1820+070 in 2–6 keV, 6–20 keV, their hardness ratio, and *Swift/BAT* light curve in 15–50 keV, from top to bottom. The black points present the data with orbital time bins (~ 92 min) and the red points shows binned data. The error bars represent 1σ statistical errors.

15–50 keV, downloaded from the “BAT Transient Monitor” website (Krimm et al. 2013)², with a time bin size of their orbital periods (~ 92 min; black points in Fig. 1). The soft and hard X-ray fluxes rapidly increased in the initial phase of the outburst, and around March 20, it reached its peak level of ~ 5 photons $\text{s}^{-1} \text{cm}^{-2}$ in 2–20 keV, corresponding to ~ 2 Crab. The source started dimming in early April, and from the middle of June, it increased its flux again. The HR was almost constant before the re-brightening. To reduce the statistical errors, we binned 1–40 adjacent data points that have similar flux levels, as shown in red in Fig. 1, and created time-averaged GSC spectra in these individual bins.

We also investigated whether or not the source was detected with *MAXI/GSC* before the 2018 outburst. We created 72-day bin light curves in 3–4 keV, 4–10 keV, and 10–20 keV, applying the image fitting technique to the GSC data from 2009 September to 2016 July, in the same manner as those adopted in the *MAXI* galactic and extragalactic X-ray source catalogs (Hori et al. 2018; Kawamuro et al. 2018b). We found, however, that the source was not detected significantly at any periods,

and estimated 3σ upper limits of the 7-year averaged fluxes as ~ 0.2 mCrab in 4–10 keV, ~ 0.1 mCrab in 3–4 keV, and ~ 1.0 mCrab in 10–20 keV.

2.1.2. *Swift* data

To acquire information at higher energies, we created hard X-ray spectra of MAXI J1820+070 from *Swift/BAT-survey* data. We processed the BAT survey data downloaded from the HEADAS archive³ via the ftool `batsurvey`, and then generated the time-averaged spectra and their response files in the individual continuous scans, using the script `make_survey_pha`. We selected the scans that partially or totally overlapped with the intervals of *MAXI/GSC* spectra, and used those scan data in the spectral analysis. If multiple BAT scans overlapping the interval of a *MAXI* spectrum were present, we adopted the one with the longest overlapping time. If there are no overlapping scans, we discarded the *MAXI* data. In the end, we obtained 63 quasi-simultaneous *MAXI/GSC* and *Swift/BAT-survey* spectra, covering the 3–200 keV band.

To investigate the more detailed spectral profile and X-ray variations on shorter time scales, we also analyzed

² <http://swift.gsfc.nasa.gov/docs/swift/results/transients>

³ <https://heasarc.gsfc.nasa.gov/FTP/swift/data/obs/>

the simultaneous *Swift*/XRT and BAT *event-by-event* data (hereafter we call BAT-event data), occasionally taken during the outburst. We picked out the observation IDs (OBSIDs) containing both XRT and BAT-event data (OBSID=00010627014, 00010627015, 00010627018, 00010627026, 00010627035, 00010627036, 00010627045, 00088657002, 00814259000, 00815603000), to create their light curves and spectra.

The OBSID=00814259000 data were acquired on March 14, 1 day after the discovery with *MAXI*, and the other datasets were taken after March 19, when the source flux almost reached its peak level. We found that all the datasets obtained after March 19 had similar spectral and temporal properties and gave similar results. In the following, we just show the results from the data with OBSID=00814259000 (hereafter Data-1) and 00010627014 (Data-2), as representative data in the beginning of the outburst and at about the first flux peak, respectively. The former observation was performed from March 14 UT 19:14:16 to 20:55:54, with net exposures of ~ 1.0 ks for the XRT and ~ 0.5 ks for the BAT, and the latter was from March 25 UT 04:07:30 to 04:23:56, with a ~ 2.4 ks exposure for the XRT and ~ 0.5 ks for the BAT. The XRT was operated in the Windowed Timing mode in both observations.

The XRT data were first reprocessed through the *ftool* `xrtpipeline` with the calibration database (CALDB) downloaded in 2018 February. Then, the source signals were extracted from a circular region with a radius of 30 pixels, centered at the source position. To avoid the pileup effects, we excluded the events in the PSF core with a radius of 5 and 15 pixels for the Data-1 and Data-2, respectively, so that the count rate is well below $150 \text{ counts s}^{-1}$ (see Evans et al. 2009). The background region of each dataset was defined as an annulus with inner and outer radii of 80 and 120 pixels, respectively, centered at the target position. We employed `swxwt0to2s6psf3_20131212v001.rmf` in the CALDB as the XRT response matrix file. The ancillary response files (ARFs) of the individual observations were created via `xrtmkarf` by considering the PSF profile.

By using the *Swift*/BAT-event data, energy spectra and light curves were produced in the standard manner as described in Sakamoto et al. (2007). We created the energy response files with the *ftool* `batdrngen` and added systematic error vectors to the spectral files with `batphasyserr`, before the spectral analysis.

2.2. Analysis and results

2.2.1. Long-term Evolution studied with *MAXI*/GSC and *Swift*/BAT-survey data

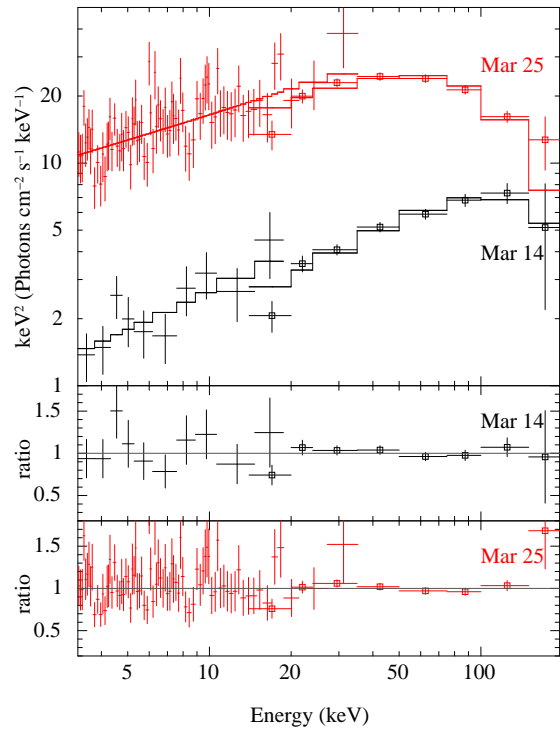


Figure 2. *MAXI*/GSC (cross) and *Swift*/BAT (open square) spectra obtained on March 14 (black) and 25 (red), with their best-fit `TBabs*nthcomp` models (top), and the data versus model ratios for the former (middle) and latter (bottom) spectra. The spectra are *unfolded* ones, corrected for the effective area of the instrument.

We first analyzed the *MAXI*/GSC and *Swift*/BAT-survey spectra to study the long-term spectral evolution, before the re-brightening in June. Figure 2 displays two typical spectra at low and high luminosities, obtained in 2018 March 14 UT 9:42–17:44 and March 25 UT 03:45–19:51, respectively. Both of them have a power-law-like profile, as usually seen in the low/hard state of BHBs. A significant spectral turnover can be seen in the March 25 spectrum at 50–100 keV, which is not very clear in the March 14 spectrum.

We applied the Comptonization model `nthcomp` to the individual GSC+BAT-survey spectra, assuming that the seed photons originate in the emission from the standard accretion disk. The `nthcomp` model calculates a Comptonized spectrum from a photon index, an electron temperature, and a characteristic temperature of the seed photons (which is the inner disk temperature T_{in} , in the case of the disk blackbody radiation). We fixed T_{in} at 0.1 keV, because it cannot be constrained in the GSC+BAT spectra, covering energies only above 3 keV. We have confirmed that the results was kept unchanged within the 90% error ranges, when $T_{\text{in}} = 0.5$ keV and 0.05 keV were adopted. To account for the interstellar absorption, we combined the `TBabs` model

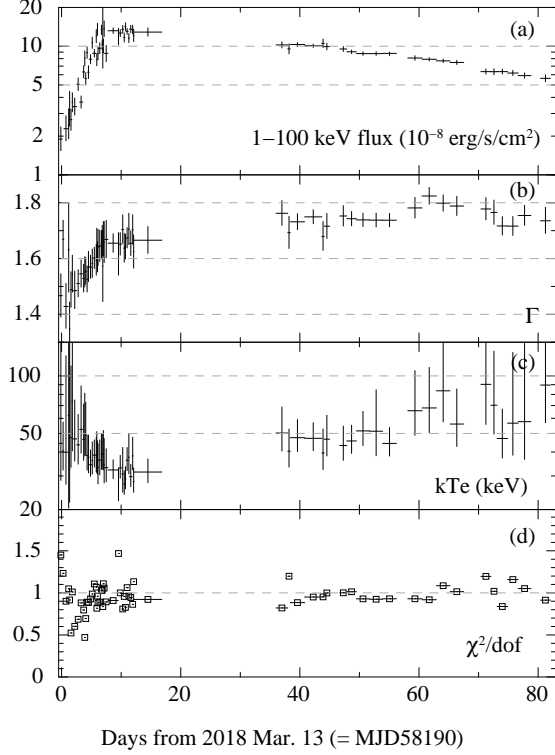


Figure 3. Time variations of the parameters in the best-fit `TBabs*nthcomp` model. The unabsorbed 1–100 keV flux in units of $10^{-8} \text{ erg s}^{-1} \text{ cm}^{-2}$, the photon index, the electron temperature in units of keV, and the reduced chi-squared, from top to bottom.

(Wilms et al. 2000), with a hydrogen column density of $1.5 \times 10^{21} \text{ cm}^{-2}$, which was determined from the *NICER* spectrum in March 12–14 (Uttley et al. 2018). We varied the cross-normalization factor of the BAT data with respect to the GSC data. We obtained ~ 1.0 with a 90% confidence range of $\pm \sim 20\%$ as its typical value.

The model well reproduced the spectra. In Fig. 2, we show the best-fit models and the data versus model ratios of the March 14 and 25 data. Figure 3 presents the overall trend in the fit parameters and the reduced chi-squared values. During the outburst rise, the electron temperature and the photon index showed a slight decrease and increase, respectively. After the flux peak, the electron temperature increased slightly, whereas the photon index nearly unchanged within the error range, during the gradual decay of the unabsorbed 1–100 keV flux by a factor of ~ 2 .

2.2.2. Short-term variation studied with *Swift*/XRT and BAT-event data

We next analyzed the simultaneous *Swift*/XRT and BAT-event data occasionally acquired in the outburst. Figure 4 presents the XRT 1-s bin light curves of MAXI J1820+070 on March 14 and 25, obtained from Data-1

and Data-2, respectively. The flux varied by a factor of ~ 2 –5 on timescales of a few to ~ 100 s in both epochs. To investigate the energy dependence of the rapid flux variation, we sorted the time bins in these light curves, in terms of their count rates. In each observation, we defined the upper and lower 30% time bins among all the data points as the high and low flux phases, respectively, and produced time-averaged spectra in these two phases (see Fig 4 for thresholds of the count rates for these phases).

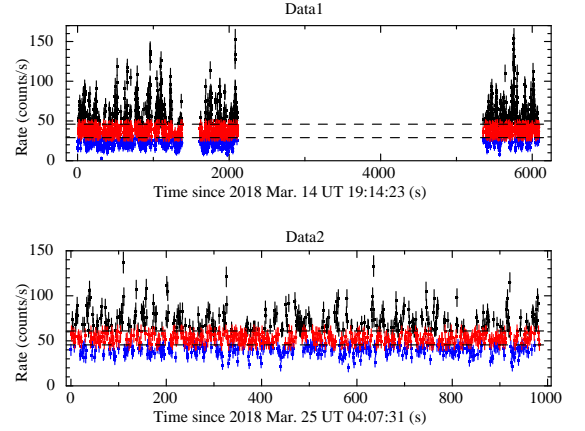


Figure 4. *Swift*/XRT light curves of MAXI J1820+070 in 0.3–10 keV obtained from Data-1 (top) and Data-2 (bottom) with 1 s bins. The dashed lines indicate the thresholds to extract the intensity-sorted spectra in Figure 6, and the black and blue points are included in high and low flux phases, respectively.

In Figure 5, we plotted the time-averaged spectra in the low- and high-intensity phases, and the ratio of the low-intensity-phase spectra with respect to the high-intensity-phase spectra, produced from the individual datasets. Both spectra in Data-1 can be approximated by a single power-law, and the spectral ratio increases with energy, indicating that the photon index in the low intensity phase is slightly lower than that in the high-intensity phase. For Data-2, both spectra show a clear spectral cutoff at around 30–50 keV. Remarkably, the low-intensity-phase spectrum displays a hump at ~ 1 keV, and the spectral ratio below ~ 2 keV decreases with increasing energy, suggesting that a less variable component than the main cut-off power-law component is present in the soft X-ray band.

We applied a Comptonization model to these intensity-sorted spectra and investigated which physical parameter(s) made the spectral differences. Here we adopted a sophisticated Comptonization model, `compps`, (Poutanen & Svensson 1996) instead of `nthcomp`. This model calculates a Comptonized spectrum produced in a hot electron cloud, based on exact numerical solutions

Table 2. Best-fit TBabs*compps and TBabs*(diskbb+compps) parameters for Data-1 and Data-2, respectively, in the high and low intensity phases

		Data-1		Data-2	
parameters		high	low	high	low
TBabs	N_{H} (10^{22} cm $^{-2}$)	$0.10^{+0.05}_{-0.04}$	< 0.1	0.12 ± 0.10	$0.15^{+0.09}_{-0.07}$
compps ^a	kT_{e} (keV)	> 240	> 48	27^{+3}_{-2}	35^{+8}_{-5}
	y-parameter	1.1 ± 0.2	$1.6^{+0.1}_{-0.2}$	0.77 ± 0.02	$0.87^{+0.03}_{-0.02}$
	kT_{bb} (keV)	0.22 ± 0.02	$0.2^{+0.2}_{-0.1}$	$0.18^{+0.12}_{-0.04}$	$0.21^{+0.05}_{-0.04}$
diskbb	norm (10^4)	8^{+4}_{-3}	$1.3^{+6.8}_{-1.0}$	53^{+90}_{-27}	17^{+22}_{-10}
	norm (10^5)	—	—	$5.3^{+41.0}_{-5.1}$	4^{+14}_{-3}
	r_{in} (km) ^b	—	—	372^{+168}_{-198}	240^{+192}_{-48}
$\chi^2/\text{d.o.f.}$		356/328	168/144	200/190	108/107
flux ^c (10^{-8} erg s $^{-1}$ cm $^{-2}$)		4.1	2.1	18	10

^aThe seed spectrum was assumed to be a disk blackbody, and the inner disk temperature of compps (kT_{bb}) was linked to that of diskbb (kT_{in}) in Data-2. The reflection component was ignored.

^bInner radius estimated from the total photons of the disk blackbody emission, including the Comptonized photons in a spherical corona (see Section 2.2.2). A distance and an inclination angle of 3 kpc and 30° are assumed, respectively. The color-temperature correction and the correction of the inner boundary condition are not considered.

^cUnabsorbed 0.01–100 keV flux.

of the radiative transfer equation, for a given electron temperature kT_{e} , Compton y-parameter, geometry of the cloud, and the energy distribution of the seed photons. We assumed spherical geometry ($\text{geom} = 4$ in the XSPEC terminology) of the Comptonization component, and a multi-color disk blackbody as the seed spectrum. We ignored the reflection component, whose strength were not constrained, likely due to the uncertainties in the cross normalization between the XRT and BAT-event spectra.

For Data-2, we combined the diskbb model (Mitsuda et al. 1984) to compps, as a direct disk blackbody component, to model the hump seen in the soft X-ray band. The inner disk temperature of diskbb, kT_{in} , was linked to the seed temperature kT_{bb} of the compps model. We also employed the TBabs model as interstellar absorption, leaving N_{H} as a free parameter. In this analysis, we varied the cross-normalization factor of the BAT with respect to the XRT, which was found to be consistent with 1.0, with a 90% error of ± 0.1 –0.2, in both Data-1 and Data-2.

These models, TBabs*(compps) and TBabs*(diskbb+compps), successfully reproduced the Data-1 and Data-2 spectra, respectively. Figure 6 shows the folded spectra with their best-fit models, and the data versus model ratio. Table 2 lists the best-fit parameters of each phase. In both datasets, the Compton y-parameters in the low

intensity phases were larger than those in the high intensity phases.

We estimated the inner disk radius for Data-2, from the photon fluxes of the direct disk component and the Comptonized component, via the equation given in (Kubota & Makishima 2004):

$$P_{\text{d}} + P_{\text{c}} \cdot 2 \cos i = 0.0165 \left[\frac{r_{\text{in}}^2 \cos i}{(D/10 \text{ kpc})^2} \right] \left(\frac{kT_{\text{in}}}{1 \text{ keV}} \right)^3 \text{ Photons s}^{-1} \text{ cm}^{-2},$$

(where P_{c} and P_{d} are photon fluxes of the Comptonized component and the direct disk component, respectively), by assuming a spherical geometry of the Comptonization component and the conservation of the number of the disk photons after Comptonization.

3. OPTICAL AND NEAR-IR DATA

3.1. Observations and data reduction

Optical and near-IR observations in the g' , R_{c} , I_{c} , r , i , z , J , H , and K_{s} bands were carried out with ground-based telescopes through the Target-of-Opportunity (ToO) program in the Optical and Infrared Synergetic Telescopes for Education and Research (OISTER). The g' -, R_{c} - and I_{c} -band data were taken with the three-color imaging system developed for the MIT-SuME project (Kotani et al. 2005; Yatsu et al. 2007; Shimokawabe et al. 2008; Yanagisawa et al. 2010) on

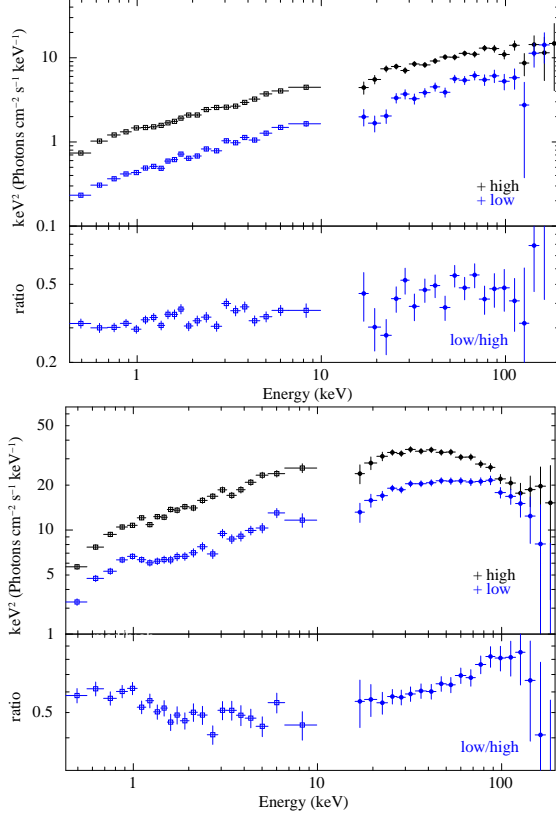


Figure 5. (Top) Simultaneous *Swift*/XRT (open square) and *Swift*/BAT (filled square) intensity-sorted spectra on March 14 (Data-1; left) and 25 (Data-2; right). They are unfolded with a power-law model having a photon index of 2. (Bottom) Ratios of the unfolded spectra in the low intensity phases with respect to those in the high intensity phases.

the MITSuME 50 cm telescope in Akeno, the 50 cm telescope at the Okayama Astrophysical Observatory (OAO) and the MURIKABUSHI 105 cm telescope at the Ishigakijima Astronomical Observatory. The r -, i - and z -band data were taken with Multi-wavelength Simultaneous High throughput Imager and polarimeter (MuSaSHI), installed on the 55 cm SaCRA telescope at Saitama University. The J -, H - and K_s -band data were taken with the Nishi-harima Infrared Camera (NIC; Ishiguro et al. 2011; Takahashi et al. 2013) on the 2.0 m Nayuta telescope at the Nishi-Harima Astronomical Observatory. The data were reduced on IRAF by following standard procedures including bias and dark subtraction, flat fielding, and bad pixel masking. Photometry was performed with IRAF. The magnitudes of MAXI J1820+070 were calibrated with nearby reference stars. The magnitudes of the reference stars were taken from the UCAC4 catalog (Zacharias et al. 2013) for the g' -, R_c - and I_c -band data, from Pan-STARRS1 Surveys (Chambers et al. 2016) for the r -,

i - and z -band data, and from the Two Micron All Sky Survey Point Source Catalog (Cutri et al. 2003) for the J -, H - and K_s -band data. The statistical photometric errors of MAXI J1820+070 and the systematic errors of the reference star magnitudes were accounted for the observational errors.

Figure 7 shows the g' , R_c , I_c -band light curves of MAXI J1820+070, together with the MAXI/GSC light curve in 2–20 keV. The optical fluxes were found to gradually increase as the X-ray flux became higher, and show significant variation in each night by 0.5–1 mag (by a factor of 1.6–2.5, in the flux unit). As described in the following section, we studied the averaged properties of the multi-wavelength spectral energy distribution (SED) around the flux peak, by combining the one-night averaged optical and near-IR data, and the quasi-simultaneous X-ray data obtained with MAXI/GSC and *Swift*/BAT. To investigate the short-term variations of the optical fluxes, and their correlation to those in X-rays, are left as a future work.

We also searched the archival optical and IR data⁴ for possible activities of MAXI J1820+070 before the 2018 outburst. The source was detected multiple times by Palomar Transient Factory (PTF) in 2013 May with R -band magnitudes of 18.3–18.7 mag and typical errors of ~ 0.06 mag. It was also detected in the mid-IR band with Wide-field Infrared Survey Explorer (WISE)/Near-Earth Object WISE (NEOWISE) in 2010 September/2014–2017 March and September. The WISE/NEOWISE apparent magnitudes were 15.3–16.3/13.7–14.8 mag with typical errors of $\sim 0.3/0.08$ mag in the W1 band ($3.4 \mu\text{m}$), and 14.7–15.4/13.4–14.6 mag with typical errors of $\sim 0.3/0.2$ in the W2 band ($4.6 \mu\text{m}$). Both the W1 and W2 band fluxes showed significant variations by 0.5–1 mag (a factor of ~ 2 in the flux unit) within a few to several days.

3.2. Analysis of Multi-wavelength SEDs

Figure 8(a) shows the multi-wavelength SED on 2018 March 24, when the g' , r , i , z , J , H , K_s -band data, together with the X-ray data from MAXI/GSC and *Swift*/BAT, were available. The X-ray data were corrected for interstellar absorption using the TBabs model with $N_H = 1.5 \times 10^{21} \text{ cm}^{-2}$ (Uttley et al. 2018), and optical/IR data for interstellar extinction using the reddden model in XSPEC with the extinction $E(B - V) = 0.26$, which was converted from the N_H value through the relation in Borlin et al. (1978). As noticed from the figure, the SED in the IR to optical band is not smoothly connected to the X-ray spectrum. For comparison, we

⁴ at <http://irsa.ipac.caltech.edu/frontpage/>.

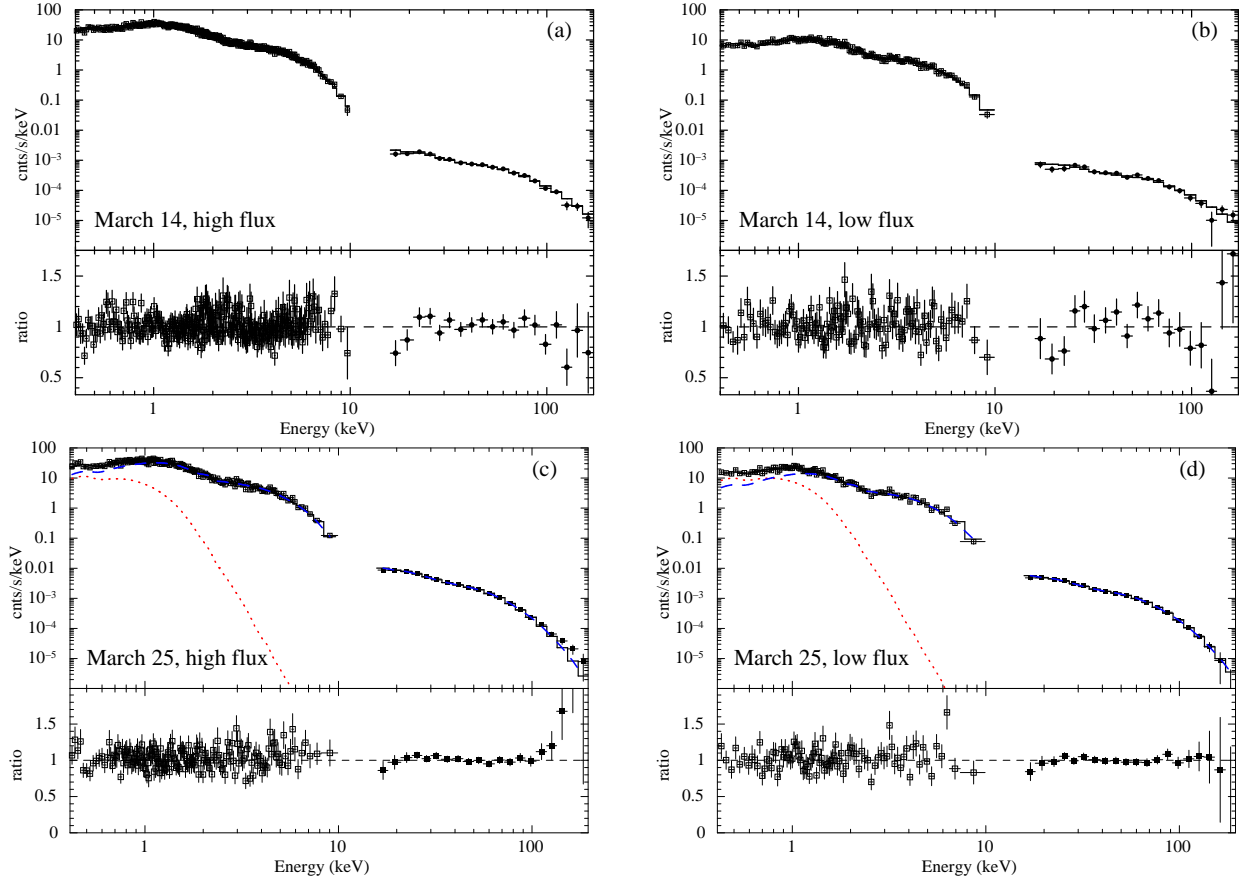


Figure 6. (a),(b) the time-averaged folded spectra in the high and low intensity phases of Data-1, and their best-fit TBabs*compps models. The lower panels present the data versus model ratio. (c),(d) same as top panels, but for Data-2 with the best-fit TBabs*(disk+compps) models. The diskbb and compps components are plotted separately with red dotted and blue dashed lines, respectively.

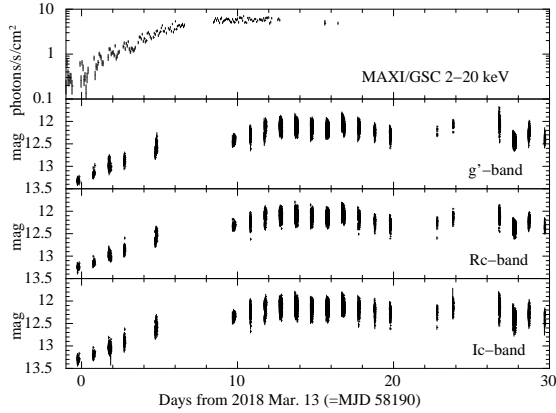


Figure 7. X-ray and optical light curves of MAXI J1820+070, obtained with MAXI/GSC and in the MIT-SuME project, respectively. The light curves in 2–20 keV, and in the optical g' , R_c , and I_c -bands are presented, from top to bottom. The magnitudes are expressed in the AB system. The error bars of the optical light curves include both the statistical photometric errors of MAXI J1820+070 and the systematic errors of the reference star magnitudes.

also plotted, in Figure 8(b), an SED obtained from the

archival optical/IR data before the 2018 outburst, and the upper limits of the X-ray fluxes estimated with the MAXI/GSC.

The optical and IR photons of BHBs can originate in the accretion disk, jet, or companion star. In the case of the disk emission, the optical and IR bands corresponds to the radiation from the outer disk region, which is often irradiated by the X-rays from the inner disk region. To obtain the upper limit of the contribution of the disk emission to the optical/IR fluxes, we applied the irradiated disk model *diskir* (Gierliński et al. 2008, 2009) to the multi-wavelength SED on 2018 March 24 (see section 4.3 for discussion of the contributions of the other emission components).

The *diskir* model computes the spectrum of the disk emission and its Comptonization, considering the irradiation of the disk. The model has 9 input parameters: the inner disk temperature kT_{in} , the photon index Γ and electron temperature kT_e of the Comptonized component, the luminosity ratio L_c/L_d of the Comptonized component to the disk component, the fraction f_{in} of

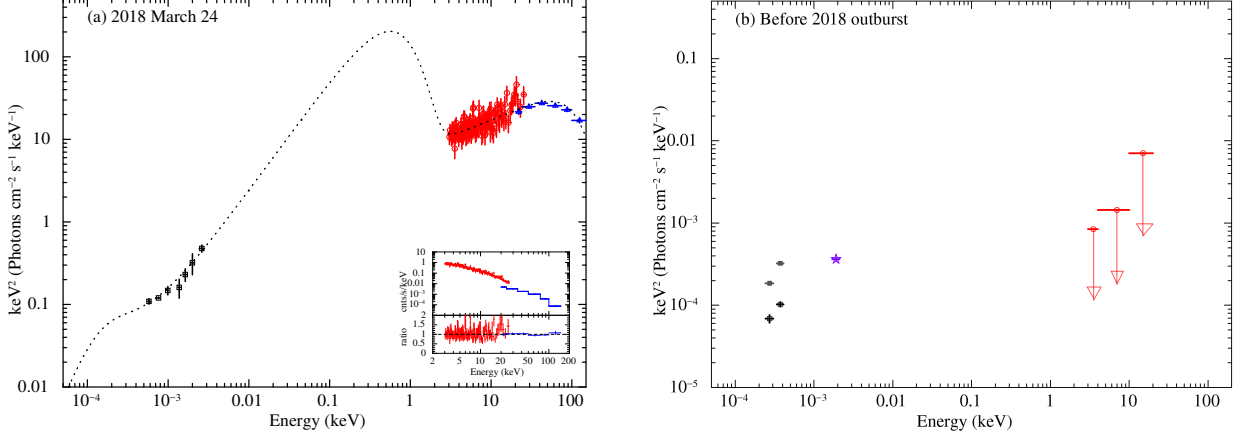


Figure 8. (a) Multi-wavelength SED of MAXI J1820+070 on 2018 March 24. The black squares indicate the optical/IR data in the K_S , H , J , z , i , r , and g' bands, from left to right. Red circles and blue triangles show the MAXI/GSC and Swift/BAT data, respectively. The best-fit `diskir` model is presented in the dotted line. The inset presents the same X-ray data folded with the instrumental responses, in units of $\text{counts s}^{-1} \text{keV}^{-1}$ (upper), and their data versus model ratio (lower). (b) SED before the start of the 2018 outburst, obtained from the archival PTF R -band data (purple star), and the WISE (black open squares)/NEOWISE (grey filled squares) IR data, combined with the 3σ upper limits of the 7-year averaged X-ray fluxes derived with the MAXI/GSC (see Section 2.1.1).

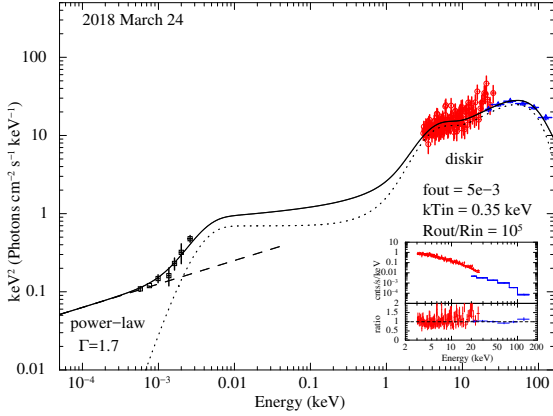


Figure 9. Same data as Fig. 8(a), with the `powerlaw+diskir` model (solid line). The power-law and `diskir` components are presented in the dashed and dotted lines, respectively.

the luminosity of the Comptonized component that is thermalized in the inner disk, the fraction f_{out} of the bolometric flux illuminating the outer disk, the radius r_{irr} of the inner disk irradiated by the Comptonized component with respect to the inner disk radius, the outer disk radius R_{out} , and the normalization, determined by the inner disk radius R_{in} in the same manner as `diskbb`.

Following previous works (e.g., Shidatsu et al. 2017), we fixed r_{irr} and f_{in} , which were unconstrained with our data, at default values, 1.1 and 0.1, respectively, which are appropriate for the low/hard state spectra (Poutanen et al. 1997). The other parameters were left as free parameters. We multiplied `TBabs` with N_{H} fixed at $1.5 \times 10^{21} \text{ cm}^{-2}$ and `redden` with $E(B - V)$ at 0.26 to the `diskir` model, as X-ray interstellar absorption and

optical/IR extinction, respectively. We have confirmed, however, that the conclusions below do not change if we increase and decrease N_{H} by a factor of 2, and change $E(B - V)$ accordingly.

As shown in Fig. 8(a), the model was able to reproduce the SED on March 24, giving a $\chi^2/\text{d.o.f.}$ value of 106/122. In this best-fit model, the reprocessed emission from the outer disk dominates the flux in the IR bands, where a profile flatter than the optical SED is seen. The parameter values were constrained to be $kT_{\text{in}} = 0.23^{+0.03}_{-0.13} \text{ keV}$, $\Gamma = 1.67^{+0.01}_{-0.03}$, $kT_{\text{e}} = 29^{+2}_{-3} \text{ keV}$, $L_{\text{c}}/L_{\text{d}} = 0.24 \pm 0.06$, $f_{\text{out}} = 6.4^{+4}_{-2} \times 10^{-5}$, and $R_{\text{out}} > 3 \times 10^4 R_{\text{in}} = 2 \times 10^7 (D/3 \text{ kpc}) (\cos i / \cos 30^\circ)^{-1/2} \text{ km}$. The Γ and kT_{e} values were consistent with those obtained in the analysis of the X-ray spectra alone, and the kT_{in} value was the same as that determined from the *Swift*/XRT and BAT-event data on March 25, within the 90% error ranges.

4. DISCUSSION

4.1. Overall X-ray Properties

Like other X-ray novae, the new X-ray source MAXI J1820+070 displayed a rapid flux rise, up to as high as ~ 2 Crab in 2–20 keV, and then a slower decay for ~ 3 months. Using MAXI/GSC data, we found that the source increased its X-ray flux $\gtrsim 4$ orders of magnitude from the quiescent level, to ~ 2 Crab in 2–20 keV band, at the peak in the end of 2018 March. Before the re-brightening in the middle of June, the source did not show any drastic spectral softening, and kept presenting a hard spectrum roughly characterized with an exponentially cut-off power-law model with a photon index

of ~ 1.5 and a cut-off energy of ~ 50 keV, which is consistent with those of black hole X-ray binaries in the low/hard state.

The observed peak flux of MAXI J1820+070 was quite high, compared with typical flux levels at which many known BHBs in the Galactic center regions show the transition to the high/soft state (~ 0.1 Crab; e.g., Yu et al. 2007; Zhou et al. 2013). This can be explained if MAXI J1820+070 is located closer to us than them. Indeed, $D \approx 3$ kpc has recently been obtained from the astrometry with Gaia data (Gandhi et al. 2018b). Using the unabsorbed 1–100 keV flux, obtained with the best-fit `nthcomp` model of the simultaneous MAXI/GSC and *Swift*/BAT spectrum on 2018 March 25, the peak luminosity in the end of March is calculated to be $\sim 2 \times 10^{38} (D/3 \text{ kpc})^2 \text{ erg s}^{-1}$, which is converted to an Eddington ratio of $L_X/L_{\text{Edd}} \sim 0.1 (D/3 \text{ kpc})^2 (M_{\text{BH}}/10 M_\odot)^{-1}$.

After the low/hard state period for ~ 3 months, the source caused re-brightening and entered into the state transition, at a luminosity similar to the first peak in March. Such a long period before the state transition is unusual in transient BHBs, although similar behavior was observed in the 2009 outburst of XTE J1752–223 (Nakahira et al. 2010), where the source stayed in the low/hard state for 3 months before the transition, with two plateau phases in its X-ray lightcurve. In that case, the complex evolution was explained by a gradual increase of the mass accretion rate for some unknown reasons.

What made the double-step rise of MAXI J1820+070 is still unclear, but possibly the first rise was caused due to an enhancement of the mass transfer from the companion star, and the second rise due to a rapid increase of the mass accretion rate caused by the disk instability that was triggered somewhere in the outer disk during the first rise and propagated inward. The viscous timescale of the disk is expressed as $t_v(R) \sim \alpha^{-1} \Omega_K^{-1} (H/R)^{-2}$, where α , H , and Ω_K are the viscosity parameter, the disk scale height, and the Keplerian angular velocity at the radius R , respectively. The time scale $t_v \sim 90$ days corresponds to $R \sim 2 \times 10^{10}$ cm for $H/R \sim 0.01$ and $\sim 4 \times 10^{11}$ cm for $H/R \sim 0.1$, when a black hole mass of $10 M_\odot$ and $\alpha = 0.1$ are assumed.

An alternative interpretation for the two-step flux increase may be provided in terms of the irradiation of the companion star, as invoked by Nakahira et al. (2014) to explain the re-flare observed in the outburst of Swift J1910.2–0546 (or MAXI J1910–057). The first flux rise could be produced by the enhancement of the mass accretion rate through the inner disk due to the disk instability, and that the strong X-rays irradiated and inflated the companion star, causing increase of the gas supply to

the accretion disk. The second flux enhancement could then be realized by triggering the disk instability again.

4.2. Implications in Long- and Short-term X-ray Variations

Looking at the MAXI/GSC and *Swift*/BAT spectra during the low/hard state in more detail, we found that the spectrum became slightly softer and bent at lower energies at higher luminosities. According to the best-fit `nthcomp` models for the individual spectra (Section 2.2.1), the photon index increased from 1.4 to 1.7 and the electron temperature decreased from 50 keV to 30 keV, during the rise phase of the outburst. This long-term spectral evolution would be explained by the change in the mass accretion rate; the standard disk is developed inwards as the mass accretion rate increases, and the soft X-rays from the standard disk cools the hot inner flow and/or corona around the standard disk, providing a softer Comptonized spectrum, with a lower electron temperature.

We also detected spectral variation on much shorter timescales, a few to ~ 100 s, using the *Swift*/XRT and BAT-event data taken on March 14 and 25, corresponding to the beginning and the peak of the outburst. In both periods, the spectrum of MAXI J1820+070 was softer/harder at high/low intensity phases of the short-term variation. Applying the `compps` model, a smaller y -parameter (and a smaller electron temperature on March 25) were obtained at higher flux phases. Similar trends were obtained in the shot analysis of Cyg X-1 (Negoro et al. 1994, 2001; Yamada et al. 2013a), and the density fluctuation in the radiation inefficient accretion flow was suggested as one possibility to drive the variation, on the basis of the evolution of the spectrum and X-ray time lags during the shots. Further studies of timing properties of MAXI J1820+070 would be required to understand the actual cause of its short-term variation.

Thanks to the good statistics of the *Swift*/XRT data, we detected, in the March 25 spectrum, a structure below ~ 2 keV that cannot be reproduced by the `TBabs*nthcomp` model and is less variable than the main Comptonization component. Assuming it as the direct disk emission component, we obtained the inner disk temperature as ~ 0.2 keV and the inner disk radius as $\sim 180\text{--}540 (D/3 \text{ kpc}) (\cos i / \cos 30^\circ)^{-1/2} \text{ km}$, which was estimated from the photon flux of the total intrinsic disk emission component, including both the direct and Comptonized ones. This radius can be converted to $\sim 12\text{--}36 R_g (M_{\text{BH}}/10 M_\odot)^{-1} (D/3 \text{ kpc}) (\cos i / \cos 30^\circ)^{-1/2}$, where $R_g = GM_\odot/c^2$, and this

means that the standard disk is truncated, around the flux peak in the end of March.

We cannot rule out, however, the possibility that the soft component seen on March 25 was not the direct standard disk emission but a Comptonized emission produced around the inner edge of the standard disk, as discussed (Chiang et al. 2010; Yamada et al. 2013b; Shidatsu et al. 2014). If this is the case, the direct disk component was below the energy range of the XRT, and the standard disk was further truncated, with a lower inner disk temperature than what we estimated above. The mass accretion rate at the flux peak can then be close to the Eddington rate, considering the radiation efficiency of the standard disk, $\sim 0.1 R_{\text{ISCO}}/R_{\text{in}}$ (where R_{in} and R_{ISCO} the radii of the inner edge of the standard disk and the innermost stable circular orbit, respectively), and the peak luminosity estimated in Section 4.1.

4.3. Origin of Optical and Near-IR Emission in the Outburst and Jet Energetics

The optical and near-IR fluxes of BHBs is considered to originate in the blackbody emission from the companion star, jet emission, and/or the emission from the outer region of the accretion disk, which is often enhanced by the irradiation of the X-rays from the inner disk region. In the case of MAXI J1820+070 during the outburst, the contribution of the companion star is negligible, because the previous PTF data suggest that the optical flux in the quiescent phase was at least ~ 3 orders of magnitude smaller than in the peak of the outburst (see Section 3.2). The multi-wavelength SED around the X-ray flux peak was technically able to be fit with an irradiated disk model. However, the resultant value of f_{out} , the strength of the reprocessed component, was unusually small compared with those of typical BHBs in the low/hard state ($> 10^{-3}$; e.g., Gierliński et al. 2009).

Considering the above results, we suggest that the optical and near-IR emission of MAXI J1820+070 in the outburst was not entirely produced by the disk emission, but substantially contributed by the jet emission, particularly in the near-IR band. Indeed, as shown in Figure 9, the SED can be fairly well reproduced, for example, by adding a power-law component (as the optically-thin synchrotron emission from jet) with a photon index of 1.7 and a normalization adjusted to the K_{S} band flux, and setting f_{out} , kT_{in} , $L_{\text{c}}/L_{\text{d}}$, and R_{out} of `diskir` to be 5×10^{-3} , 0.35 keV, 70, and $10^5 R_{\text{in}}$, respectively. In this model, the inner disk region is efficiently irradiated by the Comptonization component dominating the X-ray luminosity, and the heated disk produces a weak hump seen around ~ 5 keV. We note that the parameters re-

lated to the irradiation of the outer disk do not significantly change by the irradiation efficiency of the inner disk alone, because they are determined from the bolometric flux. Remarkably, the stronger contribution of the jet component at longer wavelengths, indicated from this model, is consistent with the observed sub-second optical variations (Gandhi et al. 2018a) likely originating in the jet activity, which was found to be stronger in redder bands.

Indeed, previous studies of BHBs suggest that steady compact jets are present during the low/hard state, and that their emission dominates the radio to IR or optical fluxes (see Fender 2010; Markoff 2010; Gallo 2010, and references therein). The SEDs of BHBs in the low/hard state exhibit a flat, power-law profile at the radio frequencies (e.g., Corbel et al. 2000; Fender 2001), with a spectral index of $\beta \sim 0$ (where the flux density $F_{\nu} \propto \nu^{\beta}$), and have a break in the sub-mm to IR band, above which a smaller β is obtained (Corbel & Fender 2002; Migliari et al. 2010; Gandhi et al. 2011; Shidatsu et al. 2011; Russell et al. 2013, 2014). As discussed also for AGN jets (Blandford & Königl 1979), this SED profile can be described with the synchrotron radiation from conical jets, where optically-thick and thin synchrotron components are observed below and above the break, respectively.

Such a broken-power-law shaped SED, extending from the radio to near-IR band, was actually obtained in MAXI J1820+070 (Russell et al. 2018) around the X-ray flux peak at the end of March, with spectral indices of $\beta \sim 0.3$ and ~ -0.7 , below and above the break frequency ν_{b} of $\sim 3 \times 10^{13}$ Hz. Following Shidatsu et al. (2011), we attempt here to estimate the physical parameters of the jet base, from ν_{b} and the flux density at ν_{b} of $F_{\nu_{\text{b}}} \sim 400$ mJy. For simplicity, we assume a single-zone jet base and ignore relativistic beaming effects by the bulk motion of the jet. If the electron number density at the Lorentz factor γ is proportional to γ^p , the synchrotron luminosity in an optically-thin part, νL_{ν} , depends on ν , p , the magnetic field strength B and the volume V of the emission region (where $V = 4\pi R^3/3$ in the case of a spherical region), and the pitch angle θ of the jet, while the synchrotron self-absorption coefficient α_{ν} is expressed as a function of ν , p , B , and θ (see Shidatsu et al. 2011, for complete expressions). The former parameter, νL_{ν} , is proportional to $\nu^{(3-p)/2}$, and thus we obtain $p = 2.4$ for MAXI J1820+070, from the observed spectral index, $\beta \sim -0.7$.

Assuming the equipartition of the magnetic field energy and the kinetic energy of electrons in the jet, and considering the condition of the optical depth and the luminosity at ν_{b} as $\sim \alpha_{\nu_{\text{b}}} R \sim 1$ and $\nu_{\text{b}} L_{\nu_{\text{b}}} \sim$

$\sim 1 \times 10^{35} (D/3 \text{ kpc})^2 \text{ erg s}^{-1}$, respectively, we obtain $B = 1 \times 10^4 (D/3 \text{ kpc})^{-0.22} (\sin \theta / \sin 30^\circ)^{0.55} \text{ G}$ and $R = 2 \times 10^9 (D/3 \text{ kpc})^{0.94} (\sin \theta / \sin 30^\circ)^{0.11} \text{ cm}$ for the jet base of MAXI J1820+070. These values are comparable to those estimated in GX 339–4 (Shidatsu et al. 2011), XTE J1550–564 (Chaty et al. 2011), and MAXI J1836–194 (Russell et al. 2014) during the low/hard state.

The magnetic energy density is derived from the above B value as $u_B = B^2/8\pi$ as $\sim 8 \times 10^6 \text{ erg cm}^{-3}$. The Lorentz factor of electrons emitting $\nu_b = 3 \times 10^{13}$ photons is ~ 10 . Following Chaty et al. (2011), we can calculate the timescales of adiabatic cooling and radiative cooling at the jet base as $\gtrsim B/c \sim 70 \text{ ms}$ and $\propto u_B^{-1} \gamma^{-1} \sim 400 \text{ ms}$, respectively. This indicates that the former is the dominant cooling process.

The total synchrotron luminosity L_{sync} is roughly estimated as $\sim 10^{36} \text{ erg s}^{-1}$, from the SED profile obtained in (Russell et al. 2018) and the energy density of the synchrotron radiation, $u_{\text{sync}} \sim L_{\text{sync}}/(4\pi R^2 c)$, is calculated to be $3 \times 10^5 \text{ erg cm}^{-3}$. The luminosity of the synchrotron self-Compton radiation, L_{SSC} , is thus estimated as $L_{\text{sync}} u_{\text{sync}}/u_B \sim 0.05 L_{\text{sync}}$. This suggests that the synchrotron self-Comptonization emission is negligible, contributing only $\sim 0.05\%$ to the X-ray flux. The energy density of external photons from the accretion disk is roughly estimated as $9 \times 10^7 \text{ erg cm}^{-3}$, from the 1–100 keV X-ray luminosity, $\sim 1 \times 10^{38} \text{ erg s}^{-1}$. The contribution of the external Comptonization emission is thus $\sim 1 \times 10^{37} \text{ erg s}^{-1}$, which is still only $\sim 10\%$ of the total X-ray luminosity. As noticed in figure 8(a), the observed near-IR fluxes are somewhat lower than what is expected from the simple extrapolation of the power-law component seen in the X-ray band, suggesting that the jet synchrotron emission itself is also unlikely to be a main contributor to the X-ray flux. These results would justify the assumption in our X-ray spectral modeling, that the X-ray photons were predominantly produced by Comptonization of the disk emission.

4.4. Implications in the Weak IR and Optical Activity Before the Outburst

We found weak optical and IR emission of MAXI J1820+070 before the start of the 2018 outburst, using the archival PTF, WISE, and NEOWISE data. The source exhibited R -band flux variation by 0.4 mag (by 0.4 in the flux unit) on a timescale of $\sim \text{day}$, and mid-IR variations by $\sim 1 \text{ mag}$ (by 2.5) on a timescale of \lesssim several days and a few years. Assuming a distance of 3 kpc, the averaged PTF apparent magnitude in the R -band, $\sim 18.5 \text{ mag}$, is converted to an absolute magnitude of $\sim 6 \text{ mag}$. This magnitude corresponds to a K-type com-

panion star, if it is a main sequence star and dominated the optical flux in the PTF observations. Because of the significant variations, however, we suggest that a large fraction of the optical and IR fluxes did not originate in the blackbody emission from the companion star, but maybe in the outer disk and/or jet emission.

5. SUMMARY AND CONCLUSION

We have studied the new BHB candidate MAXI J1820+070 utilizing X-ray data from *MAXI* and *Swift* and optical/near-IR data taken in the OISTER collaboration. What we have found can be summarized as follows.

1. The source stayed in the low/hard state for ~ 3 month, since its discovery in 2018 March until the start of the second brightening in the middle of June.
2. The X-ray spectrum in that period was successfully described with the Comptonization of the disk emission in the hot inner flow or corona with electron temperature of $\sim 50 \text{ keV}$.
3. The source showed X-ray short-term variation on timescales of seconds, which is likely associated with a change in the properties of the Comptonized cloud.
4. The source exhibited weak activity in the optical and near-IR bands before the 2018 outburst, when the source was not detected in X-rays.
5. In the outburst, its optical and near-IR fluxes were correlated with the X-ray flux. By modeling the multi-wavelength SED at the X-ray flux peak in the end of March, the optical and near-IR fluxes were found likely to be contributed by the jet synchrotron emission.

This research has made use of *MAXI* data provided by RIKEN, JAXA and the *MAXI* team. Part of this work was financially supported by Grants-in-Aid for Scientific Research 16K17672 (MS), 17H06362 (YU, HN, NK), 16K05301 (HN), and JP16J05742 (YT) from the Ministry of Education, Culture, Sports, Science and Technology (MEXT) of Japan. This work was supported by Optical and Near-Infrared Astronomy Inter-University Cooperation Program and the joint research program of the Institute for Cosmic Ray Research (ICRR), and by JSPS and NSF under the JSPS-NSF Partnerships for International Research and Education (PIRE; RI) and

Academy for Global Leadership (AGL) of Tokyo Institute of Technology (YT).

Facilities: MAXI(GSC), Swift(XRT and BAT)

REFERENCES

- Bahramian, A., Strader, J., Dage, K. 2018, ATel #11424
- Baglio, M. C., Russell, D. M. & Lewis, F. 2018, ATel #11418
- Berdyugin, A., Beledina, A., Kosenkov, I., et al. 2018, ATel #11445
- Bozzo, E., Savchenko, V., Ferrigno, C., et al. 2018, ATel #11478
- Blandford, R. D., & Königl, A. 1979, ApJ, 23 2, 34
- Bohlin, R. C., Savage, B. D., & Drake, J. F. 1978, ApJ, 224, 132
- Bright, J., Fender, R. & Motta, S. 2018, ATel #11420
- Casella, P., Vincentelli, F., O'Brien, K., et al. 2018, ATel #11451
- Chambers, K. C., Magnier, E. A., Metcalfe, N., et al. 2016, arXiv:1612.05560
- Chaty, S., Dubus, G., & Raichoor, A. 2011, A&A, 529, A3
- Chang, C. Y., Done, C., Still, M., & Godet, O. 2010, MNRAS, 403, 1102
- Corbel, S., Fender, R. P., Tzioumis, A. K., et al. 2000, A&A, 359, 251
- Corbel, S., & Fender, R. P. 2002, ApJ, 573, L35
- Cutri, R. M., Skrutskie, M. F., van Dyk, S., et al. 2003, "The IRSA 2MASS All-Sky Point Source Catalog, NASA/IPAC Infrared Science Archive"
- Del Santo, M., & Segreto, A. 2018, ATel #11427
- Denisenko, D. 2018, ATel #11400
- Done, C., Gierliński, M., & Kubota, A. 2007, A&A Rv, 15, 1
- Evans, P. A., Beardmore, A. P., Page, K. L., et al. 2009, MNRAS, 397, 1177
- Fender, R. P. 2001, MNRAS, 322, 31
- Fender, R. 2010, in The Jet Paradigm, Lecture Notes in Physics. Springer-Verlag Berlin, 794, 115
- Floers, A., Taubenberger, S., Vogl, C., et al. 2018, ATel #11480
- Gallo, E. 2010, in The Jet Paradigm, Lecture Notes in Physics. Springer-Verlag Berlin, 794, 85
- Gandhi, P., Blain, A. W., Russell, D. M., et al. 2011, ApJL, 740, L13
- Gandhi, P., Paice, J. A., Littlefair, S. P., et al. 2018, ATel #11437
- Gandhi, P., Rao, A., Johnson, M. A. C., Paice, J. A., & Maccarone, T. J. 2-18, ArXiv:1804.11349
- Garnavich, P., & Littlefield, C. 2018, ATel #11425
- Gehrels, N., Chincarini, G., Giommi, P., et al. 2005, ApJ, 621, 558
- Gierliński, M., Done, C., & Page, K. 2008, MNRAS, 388, 753
- Gierliński, M., Done, C., & Page, K. 2009, MNRAS, 392, 1106
- Homan, J., Uttley, P., Gendreau, K., et al. 2018, ATel #11820
- Hori, T., Shidatsu, M., Ueda, Y., et al. 2018, ApJS, 235, 7
- Ishiguro, M., Takahashi, J., Zenno, T., Tokimasa, N., & Kuroda, T. 2011, Annu. Rep. Nishi-Harima Astron. Obs., 21, 13
- Kawamuro, T., Negoro, H., Yoneyama, T., et al. 2018, ATel #11399
- Kawamuro, T., Ueda, Y., Shidatsu, M., et al. 2018, ApJS, in press
- Kennea, J. A., Marshall, F. E., Page, K. L., et al. 2018, ATel #11403
- Kennea, J. A., & Siegel, M. H. 2018, ATel #11404
- Kennea, J. A. 2018, ATel #11406
- Kotani, T., Kawai, N., Yanagisawa, K., et al. 2005, Nuovo Cimento C Geophysics Space Physics C, 28, 755
- Krimm, H. A., Holland, S. T., Corbet, R. H. D., et al. 2013, Arxiv:1309.0755
- Kubota, A., & Makishima, K. 2004, ApJ, 601, 428
- Kuulkers, E., Bozzo, E., Ferrigno, C., Belloni, T., Sanchez-Fernandez, C. 2018, ATel #11490
- Littlefield, C. 2018, ATel #11421
- Magdziarz, P., & Zdziarski, A. A. 1995, MNRAS, 273, 837
- Markoff, S. 2010, in The Jet Paradigm, Lecture Notes in Physics. Springer-Verlag Berlin, 794, 142
- Mandal, A. K., Singh, A., Stalin, C. S., Chandra, S., & Gandhi, P. 2018a, ATel #11458
- Mandal, A. K., Singh, A., Stalin, C. S., Chandra, S., & Gandhi, P. 2018b, ATel #11462
- Matsuoka, M., Kawasaki, K., Ueno, S., et al. 2009, PASJ, 61, 999
- McClintock, J. E., & Remillard, R. A. 2006, in Compact Stellar X-Ray Sources, ed. W. H. G., Lewin, & M. van der Klis (Cambridge: Cambridge Univ. Press), 157
- Mereminskiy, I. A., Grebenev, S. A., Molokov, S. V., et al. 2018, ATel #11488

- Migliari, S., Tomsick, J. A., Miller-Jones, J. C. A., et al. 2010, *ApJ*, 710, 117
- Mihara, T., Nakajima, M., Sugizaki, M., et al. 2011, *PASJ*, 63, 623
- Mitsuda, K., Inoue, H., Koyama, K., et al. 1984, *PASJ*, 36, 741
- Munoz-Darias, T., Jimenez-Ibarra, F., Armas Padilla, M., Casares, J., & Torres, M. A. P. 2018, *ATel* #11481
- Nakahira, S., Yamaoka, K., Sugizaki, M., et al. 2010, *PASJ*, 62, L27
- Nakahira, S., Ebisawa, K., Negoro, H., et al. 2013, *Journal of Space Science Informatics*, 2, 29
- Nakahira, S., Negoro, H., Shidatsu, M., et al. 2014, *PASJ*, 66, 84
- Negoro, H., Miyamoto, S., & Kitamoto, S. 1994, *ApJL*, 423, 127
- Negoro, H., Kitamoto, S., & Mineshige, S. 2001, *ApJ*, 554, 528
- Negoro, H., Kohama, M., Serino, M., et al. 2016, *PASJ*, 68, 1
- Paice, J. A., Gandhi, P., Page, K., et al. 2018, *ATel* #11432
- Poutanen, J., & Svensson, R. 1996, *ApJ*, 470, 249
- Poutanen, J., Krolik, J. H., Ryde, F. 1997, *MNRAS*, 292, L21
- Russell, D. M., Markoff, S., Casella, P., et al. 2013, *MNRAS*, 429, 815
- Russell, T. D., Soria, R., Miller-Jones, J. C. A., et al. 2014, *MNRAS*, 439, 1390
- Russell, D. M., Baglio, M. C., Bright, J., et al. 2018, *ATel* #11533
- Sakamoto, T., Hill, J. E., Yamazaki, R., et al. 2007, *ApJ*, 669, 1116
- Sako, S., Ohsawa, R., Ichiki, M., et al. 2018, *ATel* #11426
- Shidatsu, M., Ueda, Y., Tazaki F., et al. 2011, *PASJ*, 63, 785
- Shidatsu, M., Ueda, Y., Yamada, S., et al. 2014, *ApJ*, 789, 100
- Shidatsu, M., Tachibana, Y., Yoshii, T., et al. 2017, *ApJ*, 850, 155
- Shimokawabe, T., Kawai, N., Kotani, T., et al. 2008, in *American Institute of Physics Conference Series*, Vol. 1000, American Institute of Physics Conference Series, ed. M. Galassi, D. Palmer, & E. Fenimore, 543–546
- Takahashi, J., Zenno, T., & Ishiguro, M. 2013, *Bull. Cent. Astron. Univ. Hyogo* 1, 1722
- Tetarenko, A. J., Bremer, M., Bright, J., et al. 2018, *ATel* #11440
- Trushkin, S. A., Nizhelskij, N. A., Tsybulev, P., G., & Erkenov, A. 2018, *ATel* #11439
- Uttley, P., Gendreau, K., Markwardt C., et al. 2018, *ATel* #11423
- Wilms, J., Allen, A., & McCray, R. 2000, *ApJ*, 542, 914
- Yamada, S., Negoro, H., Torii, S., et al. 2013a, *ApJL*, 767, 34
- Yamada, S., Makishima, K., Done, S., et al. 2013b, *PASJ*, 65, 80
- Yanagisawa, K., Kuroda, D., Yoshida, M., et al. 2010, *American Institute of Physics Conference Series*, 1279, 466
- Yatsu, Y., Kawai, N., Shimokawabe, T., et al. 2007, *Physica E Low-Dimensional Systems and Nanostructures*, 40, 434
- Yu, W., Lamb, F. K., Fender, R., & van der Klis, M. 2007, *ApJ*, 663, 1309
- Yu, W., Zhang, J., Yan, Z., Wang, X., & Bai, J. 2018, *ATel* #11510
- Zacharias, N., Finch, C. T., Girard, T. M., et al. 2013, *AJ*, 145, 44
- Zhou, J. N., Liu, Q. Z., Chen, Y. P., et al. 2013, *MNRAS*, 431, 2285